MOF-based DNA hydrolases optimized by atom engineering for the removal of antibiotic-resistant genes from aquatic environment

Ge Fang [a,1], Ruonan Kang [a,1], Yu Chong [a], Liming Wang [b], Chuanqiang Wu [c], Cuicui Ge [a,*]

[a] *State Key Laboratory of Radiation Medicine and Protection, School of Radiation Medicine and Protection, School for Radiological and Interdisciplinary Sciences (RAD-X), Collaborative Innovation Center of Radiation Medicine of Jiangsu Higher Education Institutions, Soochow University, Suzhou 215123, China*
[b] *CAS Key Laboratory for Biomedical Effects of Nanomaterials and Nanosafety, Institute of High Energy Physics, Chinese Academy of Sciences, Beijing 100049, China*
[c] *Institutes of Physical Science and Information Technology, Anhui University, Hefei, Anhui 230601, China*

A B S T R A C T

In this study, the spatial location effect of the incorporated metal atoms on the hydrolysis activity of metal organic framework-based nanomaterials (MOFs) was investigated. UiO-type MOFs incorporated with single-atom Cu at different spatial positions were prepared and their hydrolysis activity towards phosphoester bonds was found to be highly depended on the location of the atomically dispersed Cu atoms. Especially, the attachment of Cu atoms to ligand (UiO-67-Cu$_N$) resulted in the most significant increase of their hydrolysis activity, which can be attributed to the elevated oxygen vacancies and increased Lewis acidity of MOFs. As a result, UiO-67-Cu$_N$ efficiently catalyzed the cleavage of DNA acting as DNA hydrolases, thereby effectively inhibiting the horizontal gene transfer of ARGs and eliminating bacterial resistance to antibiotic. This study opens up new prospects for the rational design of high-performance MOF-based DNA hydrolases and developing new treatment strategies for the removal of ARGs.

1. Introduction

With the increased usage of antibiotics, antibiotic-resistant genes (ARGs) are now ubiquitous in various natural environments, including municipal solid waste leachate, sludge, sediments, wastewater, and even drinking water. [1–3] Moreover, the dissemination of ARGs in the environment has seriously threatened ecological environment and human health. [4–6] Therefore, it is crucial to remove the ARGs in environment and inhibit the horizontal transfer (HGT) of ARGs for controlling the spread of ARGs in the environment. Traditional treatment technologies [7] such as chlorination [8] and ultraviolet irradiation, [9] Fenton oxidation, [10] and photocatalytic oxidation, [11,12] are not ideal for the removal of ARGs from aquatic environment, with the raised concern on high dose of disinfectants, generation of disinfection byproducts, and enhancement of the abundances and diversity of ARGs. [13,14] Thus, there is a compelling need to explore new treatment approaches for efficient removal of ARGs in the environment.

Recently, carbon-based and cerium-based nanomaterials have been found to cleave DNA through mimicking the activity of phosphatase, photolyase, and topoisomerase I. [15,16] However, carbon-based

nanomaterials are actually able to cleave DNA with the help of light. [17] As for CeO$_2$ nanoparticles, the product inhibition effect was inevitably encountered. [18,19] Metal organic frameworks (MOFs) containing Lewis acid metal have attracted attention as phosphatase mimics, which have been widely studied for the decomposition of organophosphorus contaminants including nerve agents and organophosphate pesticide. [20–24] However, the cleavage effect of MOFs on the phosphodiester linkage has rarely been reported. Based on this background, it is promising to explore the effect of MOFs on DNA cleavage and optimize their hydrolytic activity. Due to their excellent aqueous stability over a wide range of pH values and the versatility of Zr-based nodes, a variety of Zr-based MOFs such as UiO-66, NU-1000 and MOF-808 have been discovered to hydrolytically cleave the P-O bonds. [25–28] Their catalytic activity is mainly due to the strongly acidic Zr^{IV} for the activation of coordinated phosphate species and numerous Lewis-acidic Zr-OH-Zr bonds, which resemble the Zn-OH-Zn active sites of natural phosphatase. [29] However, the hydrolytic activity of Zr-based MOF toward P-O bonds remains unsatisfied. [30]

Tremendous efforts have been devoted to exploring novel strategies to enhance the hydrolytic activity of Zr-based MOF. [31,32]

Particularly, some progress has been achieved by introducing Lewis-acidic metal ion like Cu^{2+}, Ce^{4+} and Zn^{2+} in the secondary building units of Zr-based MOFs to endow them with excellent hydrolytic activity. [33,34] For example, Farha's group revealed that the catalytically hydrolytic activity of UiO-66 toward the phosphonate ester chemicals could be remarkably enhanced after the introduction of Ce^{IV} in the metal node, originated from the superior Lewis acidity of Ce(IV) to Zr(IV) in homogeneous conditions and the increased interaction between P=O bonds and Ce(IV) 4 f oribtals. [35] Zhang et al. reported that Zr-MOF with anchored Fe(III) on the skeleton achieved the efficient and selective hydrolysis of methoxyfurfural to levulinic acid through narrowing the pore size. [36] However, a comprehensive investigation on how the spatial position of the introduced metal sites influences the hydrolytic performance of MOF-based nanozymes has rarely reported. Especially, Carlos Marti-Gastaldo's group have demonstrated that precise controlling the atom distribution of the introduced metal sites at an atomic scale would endow the heterometallic organic framework with excellent chemical stability and the improved catalytic performance based on synergetic cooperation. [37,38] Thus, it would be highly desirable to gain fundamental understanding on the spatial-position effects of the incorporated metal sites at the atomic scale in the MOFs on their catalytic activity.

In this regard, we designed a series of UiO-66/UiO-67 decorated by single-atom Cu at different locations for the hydrolysis of phosphoester bonds and demonstrated the correlation between the position of the introduced catalytic site and their catalytically hydrolytic activity (Scheme 1 A). The different position of the introduced catalytic sites by this versatile MOF platform engendered different oxygen vacancies and Lewis acidity, which accounted for the significant difference in hydrolytic performance of these MOFs. Furthermore, the screened single-atom-Cu-decorated UiO-type MOFs with the highest hydrolytic activity was applied to catalytically hydrolyze both single and double strand DNA (Scheme 1 B). Additionally, the MOF-based hydrolases showed outstanding environmental tolerance and high stability, and it is easy to

be separated and recycled, indicating that the MOF-based nanozymes can potentially be considered as a replacement for natural hydrolase in practical applications. Next, we investigated the effect of single-atom Cu decorated UiO-type MOFs on the HGT of ARGs. This work may provide theoretical guidance on designing MOFs-based nanomaterials with high cleavage performance toward DNA and developing MOF-based DNA hydrolase for the removal of ARG, which might be helpful to develop more advanced treatment technologies for controlling ARGs pollution.
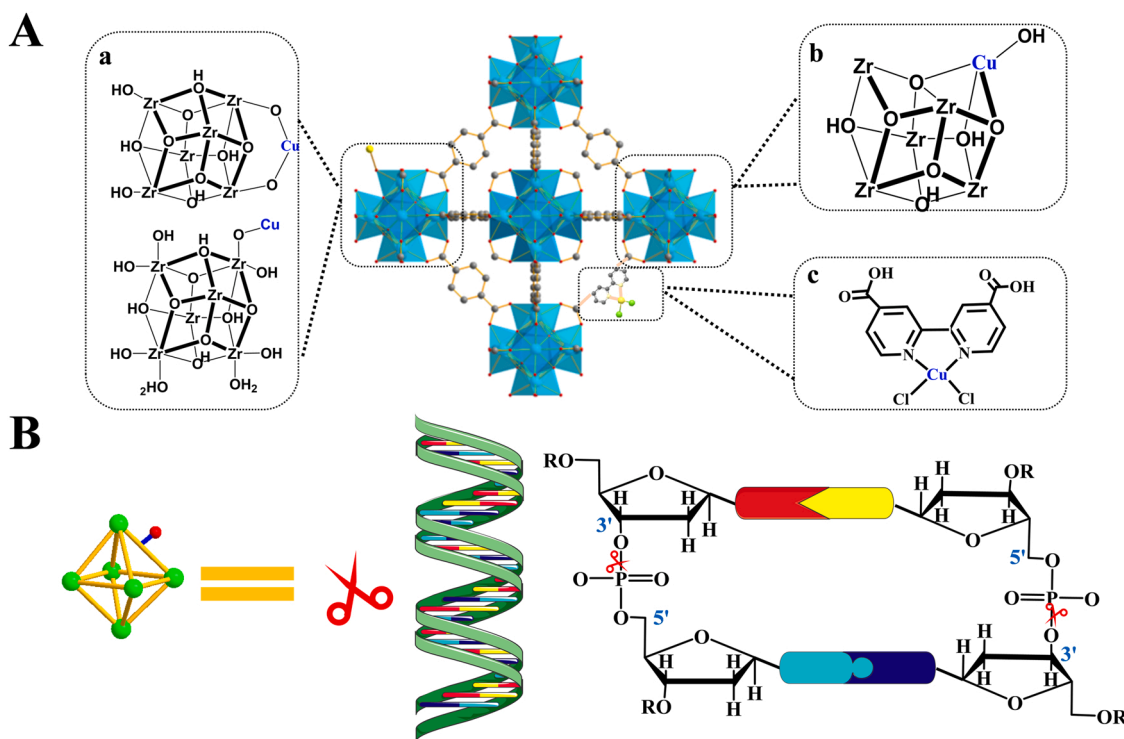
2. Materials and methods

2.1. Materials

Zirconium tetrachloride ($ZrCl_4$, 98%) was purchased from Meryer (Shanghai) Chemical Technology Co., Ltd. Terephthalic acid (TA, 98%), 2, 2-Bipyridine-4, 4'-dicarboxylic acid (bpydc, 98%) and copper(II) chloride dihydrate ($CuCl_2 \cdot 2H_2O$, 98%) were achieved from Sigma Aldrich. N, N-dimethylformamide (DMF, 99.9%) and Bis(4-nitrophenyl) phosphate (BNPP, 99%) was obtained from Aladdin. Dimethyl 4-nitrophenyl phosphate (DMNP, 99%) was obtained from J&K Chemical Co., Ltd. Tetrahydrofuran (THF, AR), acetic acid (37 wt%) and methanol (AR) were purchased from Shanghai Chemical Reagent Company. All chemicals were used without further treatment.

2.2. Preparation and characterizations of a series of single atom Cu-decorated UiO-type MOFs at different locations

Cu/UiO-66 was fabricated through a solvothermal method according to the previous literature. [39] UiO-66 powder (20 mg) and $CuCl_2 \cdot 2H_2O$ (24 mg) were dissolved in 4 mL of DMF. The mixture was stirred for another 20 min, and then heated at an 85 °C oven for 24 h. Unlike the synthesis of Cu/UiO-66 and UiO-67-Cu_N, the Cu_{ex}-UiO-66 was prepared *via* a one-step hydrothermal synthesis. Zirconium tetrachloride (33.4 mg, 0.039 mmol), terephthalic acid (25 mg, 0.055 mmol) and

Scheme 1. Schematic illustration of the synthesized UiO-type MOFs and the potential application for the cleavage of DNA. (A) Schematic representation of the construction of a series of single-atom Cu decorated UiO-type MOFs and the detailed atomic structure of model units of Cu/UiO-66 (a), Cu_{ex}-UiO-66 (b) and UiO-67-Cu_N (c). (B) The UiO-67-Cu_N showed excellent DNA cleavage performance through the hydrolysis of the phosphodiester linkage.

CuCl$_2$.2H$_2$O (33.6 mg, 0.054 mmol) were dissolved in 10 mL of DMF. The mixture was stirred for 20 min and transferred into a 120 °C oven for 24 h. The synthesis of UiO-67-Cu$_N$ was similar to that the synthesis of Cu/UiO-66. In a 50 mL round-bottom flask, 30 mg of UiO-67-bpydc and 4.84 mg of CuCl$_2$.2H$_2$O were dissolved in 10 mL of THF, followed by sonication for 20 min. After stirring for 2 h at room temperature, the synthesis process was finished. All of the as-synthesized initial products were collected by centrifugation (10,000 rpm, 10 min), and washed four times with methanol. Finally, the product was dried under vacuum overnight at 60 °C.

The morphology of the as-fabricated MOFs was characterized by Transmission Electron Microscope (TEM, Tecnai G2 spirit BioTwin, FEI, USA). The crystallinity of sample was characterized by powder X-ray diffraction (PXRD) on a Bruker D8 Advance diffractometer equipped with Cu Kα radiation (λ = 1.5406 Å). Energy-dispersive X-ray spectroscopy (EDX) elemental mapping was performed using a Talos F200X microscope (FEI, USA). The X-ray absorption spectra of Cu K-edge (8978 eV) were measured at the XRD station of beamline 4B9A of BSRF in transmission mode, with corresponding metal foils, CuO and Cu$_2$O as the reference for energy calibration as well as data analysis. The X-ray photoelectron spectroscopy (XPS) analyses were carried out with a Thermo ESCALAB 250Xl spectrometer (Thermo-Fisher Scientific, USA) using monochromatic Al Kα X-Ray source (1486.6 eV). The concentrations of Zr and Cu of the as-fabricated MOFs were quantified by inductively coupled plasma optical emission spectroscopy (ICP-OES, ICAP7200, Thermo Fisher, Germany). The electron paramagnetic resonance (EPR) experiments were conducted at room temperature using an EPR spectrometer (Bruker E500, Bruker, Germany). The Fourier transform infrared spectra (FTIR) were obtained by Fourier transformed infrared spectrometer (Nicolet iS 50, Thermo Electron Scientific, USA). The ^{1}H-nuclear magnet resonance (^{1}H NMR) spectra were recorded using 700 MHz Bruker Ascend 700 spectrometers, and D$_2$O was used as the deuterated solvent.

2.3. Evaluating the hydrolysis activity toward DMNP by MOF-based Nanozymes

Firstly, 1 mg of a series of UiO-type MOFs was dispersed in 1 mL of Tris-HCl buffer solution (50 mM, pH=9), followed by introducing the DMNP at a range of concentrations. Then, the absorption spectra of the mixture solution were monitored by a UV spectrometer (UV-3600, Shimadzu, Japan) every 5 min for a total of 30 min. The kinetic parameters can be calculated according to the following equation:

$$v = V_{max} \times [S]/(K_m + [S])$$

where v represents the initial velocity and V_{max} is defined as the maximum reaction velocity. [S] is the concentration of the substrate, and K_m represents the Michaelis constant.

2.4. Environmental adaptability of a series of Cu single atom-decorated UiO-type MOFs and Alkaline phosphatase (ALP)

The pH stability of and natural ALP were compared by the following procedure. A certain amount of ALP or MOFs was incubated with DMNP at varying pH (2.0–10.0) at 37 °C for 30 min. The temperature tolerance of the MOF-based nanozyme and ALP was studied in the temperature range of 4–100 °C for 15 min, and the activity of the sample at 4 °C was taken as the control. The storage stability was determined by measuring the residual activity of ALP or nanozyme. The MOF-based nanozymes were recycled by centrifugation. As for natural ALP, the reaction systems containing ALP and DMNP were stored at room temperature and their enzymatic activity was measured every day. The UV-Vis spectroscopy (UV-3600, Shimadzu, Japan) was applied for the determination of the enzyme-like activities.

2.5. DNA cleavage activity of UiO-67-Cu$_N$

2.5.1. Single-stranded DNA cleavage by UiO-67-Cu$_N$

All the DNA oligomers were achieved from Sangon Biotech (Shanghai) Co., Ltd and the fluorescent label of FAM was modified at the 3′ or 5′ ends of the DNA strand (Table S4). Each DNA sample was dissolved in deionized water to a final concentration of 1.0 μM in the presence of UiO-66, UiO-67-bpydc and UiO-67-Cu$_N$, respectively. The incubation system was maintained at 60 °C for 5 h. After that, the cleavage products were separated using 15% denaturing polyacrylamide gel electrophoresis (dPAGE) and the electrophoretic images were analyzed using a ChemDoc MP imaging system (Bio-Rad, USA). Finally, the relative cleavage efficiency of MOFs was quantitated with ImageJ software. All experiments were performed in triplicate.

2.5.2. Plasmid DNA cleavage by UiO-67-Cu$_N$

The plasmid DNA was extracted using a SanPrep Column Plasmid Mini-Preps Kit (Sangon Biotechnology, China) according to the protocol recommended by the manufactures. The purity and the concentration of the extracted plasmid DNA were characterized using agarose gel electrophoresis and a Biodrop Spectrophotometer (Thermo Fisher Scientific, USA), respectively. Each plasmid DNA sample was dissolved in deionized water to a final concentration of 80 ng· mL^{-1} in the presence of a range of concentrations of UiO-67-Cu$_N$ (0.1, 0.3, 0.5, 1 mg·mL^{-1}) at 37 °C for 5 h. After that, the cleavage products were separated using agarose gel electrophoresis and the electrophoretic images were analyzed using a ChemDoc MP imaging system (Bio-Rad, USA). Finally, the relative cleavage efficiency of MOFs was quantitated with ImageJ software. All experiments were performed in triplicate. Meanwhile, the surface topography of the plasmids after different treatment was observed using the atomic force microscope (AFM, Icon, Bruker, Germany) Similarly, the effects of ions on the DNA cleavage activity of UiO-67-Cu$_N$ were measured through subjecting the MOFs to different metal ions (NaCl, KCl, MgCl$_2$, CaCl$_2$) and salt ions (NaCl, Na$_2$CO$_3$, Na$_2$SO$_4$, NaNO$_3$) with the concentration of 2 M. In addition, we also investigated the DNA cleavage activity of UiO-67-Cu$_N$ in real water samples, which was obtained from dushu lake in Suzhou city, China.

2.5.3. Reusability of a series of Cu single atom-decorated UiO-66

To test the recycling ability of MOF-based nanozymes, each DNA sample was dissolved to a final concentration of 8 μg/mL containing 1 mg of the MOFs. The mixed system was maintained at 37 °C for 5 h. After each reaction cycle, the MOFs were collected by centrifugation (10,000 rpm, 5 min), and then washed with ultrapure water and collected again. The MOFs was then subjected to the next catalytic cycle.

2.6. The extraction and cleavage of ARGs-carrying plasmid DNA

2.6.1. Induction of the antibiotic resistance in E. coli to Penicillin

The induced Penicillin-resistant E. coli cells were acquired through a long-term exposure to gradually increased concentrations of Penicillin sodium. [40] In detail, 100 μL of E. coli cells (10^8 CFU·mL^{-1}) at the logarithmic phase were transferred into 5 mL of Luria Bertani (LB) medium containing 0.5 MIC of Penicillin. Meanwhile, the E. coli cells cultured in normal LB medium were selected as the control group. The OD$_{600}$ of bacterial suspension was measured to monitor the bacterial proliferation per 24 h. Once the bacterial concentration reached 85% of the control group, we defined that the bacteria had been adapted to the concentration of the tested Penicillin and then the exposure dose was doubled. Otherwise, the concentration of Penicillin was sustained for another 24 h growth. The above evolution procedure was repeated at 24 h intervals for a gradient increment of antibiotic concentration at 32, 64, 128, 256, and 512 μg·mL^{-1}. We defined the resistance of E. coli to Penicillin as an increased MIC over 512 μg·mL^{-1}, a more than 16-fold increase compared to the original MIC of E. coli cells. After 30-day selections, the resistance of E. coli cells to Penicillin were obtained and

stored in LB liquid medium containing sterile glycerol at − 80 °C.

2.6.2. *The cleavage of ARGs-carrying plasmid DNA by UiO-67-Cu$_N$*

The ARGs-carrying plasmid DNA was extracted from Penicillin-resistant *E. coli* using a SanPrep Column Plasmid Mini-Preps Kit (Sangon Biotech, Shanghai) according to the protocol recommended by the

manufactures. The purity and concentration of the extracted plasmid DNA were measured through agarose gel electrophoresis and Biodrop Spectrophotometer (Thermo Fisher Scientific, USA), respectively. Each ARGs-carrying plasmid DNA sample was dissolved in deionized water to a final concentration of 80 ng/mL in the presence of a range of concentrations of UiO-67-Cu$_N$ (0.1, 0.3, 0.5, 1 mg·mL^{-1}) at 37 °C for 5 h.
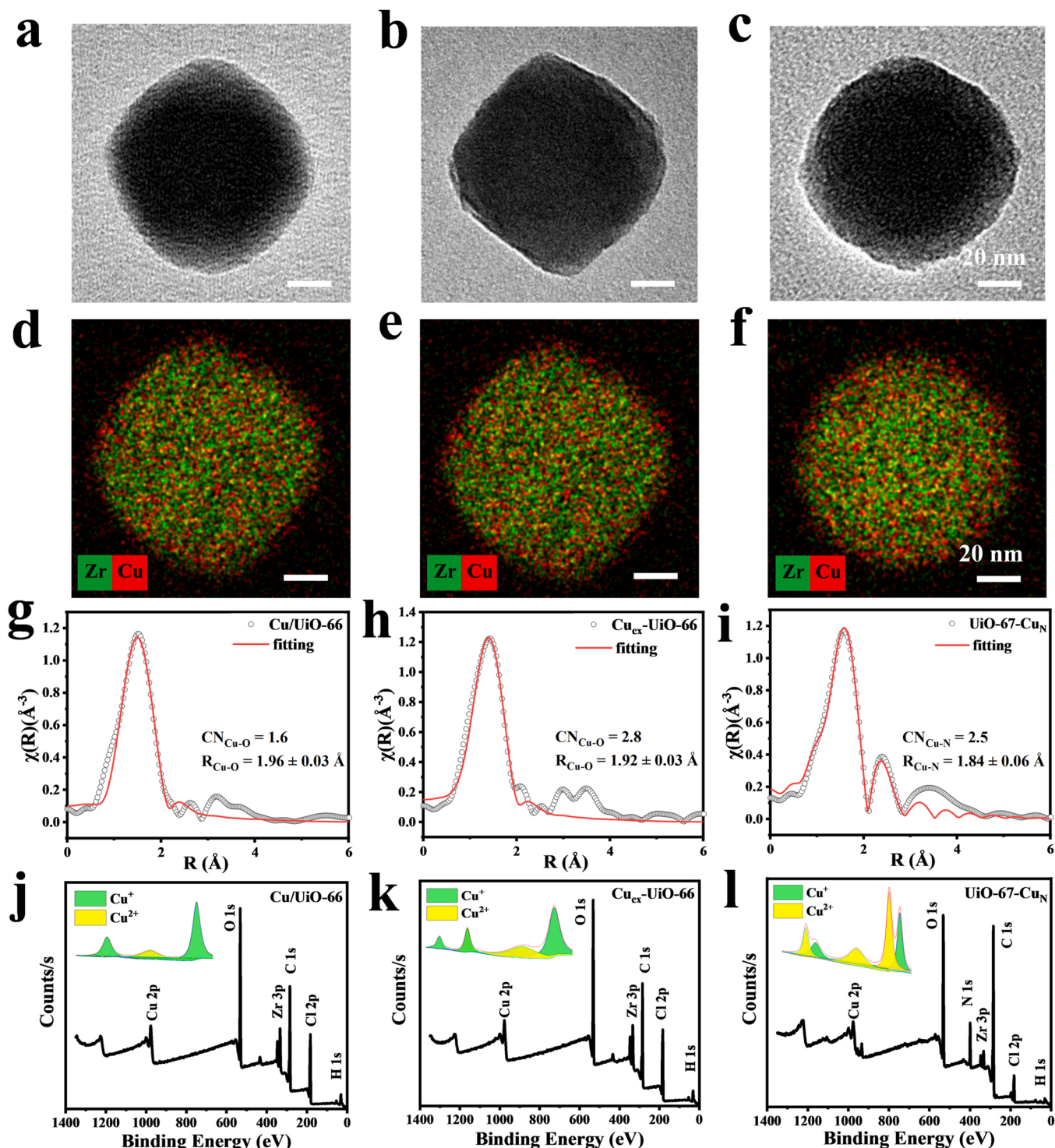

Fig. 1. Characterization of a series of Cu single atom-decorated UiO-66/UiO-67. (a-f) TEM images and the corresponding STEM-EDX elemental mapping images of an individual Cu/UiO-66 (a&d), Cu$_{ex}$-UiO-66(b&e), and UiO-67-Cu$_N$(c&f), respectively. (g-i) Cu K edge EXAFS fitting results of Cu/UiO-66 (g), Cu$_{ex}$-UiO-66 (h), and UiO-67-Cu$_N$ (i). The black open circles showed the original data of the EXAFS spectra while the red lines were the fitting results of the spectra. The y-axis is the intensity of k3 weight Fourier transformation. (j-l) The XPS spectra of Cu/UiO-66 (j), Cu$_{ex}$-UiO-66 (k), and UiO-67-Cu$_N$ (l). The inset showed the corresponding XPS spectra of MOFs in the Cu 2p region.

After that, the cleavage products were separated using agarose gel electrophoresis and the electrophoretic images were analyzed using a ChemDoc MP imaging system (Bio-Rad, USA). Finally, the relative cleavage efficiency of MOFs was quantitated with ImageJ software. All experiments were performed in triplicate.

2.7. The inhibitory effect of UiO-67-Cu_N on the transformation of ARGs

According to the transformation experiment in the reference, firstly, a series of different concentration of UiO-67-Cu_N were mixed with 100 ng of the ARGs-carrying plasmids and then 100 μL of competent cells (*E. coli*, ATCC 8739) suspension were transferred into the mixture. The sample tube was gently shaken and then maintained in a 42 °C water bath for 90 s, followed by putting into an ice-water bath for 3 min. Finally, 2 mL of LB medium were added to the sample tube and incubated at 37 °C for 2 h. After the incubation, 100 μL of the mixtures were spread evenly on the surfaces of LB agar plates containing 167 U·mL^{-1} of penicillin and the plates were incubated at 37 °C for 24 h. Then the obtained *E. coli* colonies were counted. The transformation efficiency and transformation frequency were respectively calculated according to the reference. The treatment without UiO-67-Cu_N was set as a control.

3. Results and discussion

3.1. Synthesis and characterization of a series of single-atom Cu decorated UiO-type MOFs

Owing to its high chemical stability and excellent tunability, UiO-type MOFs were chosen for this proof-of-concept study. A series of UiO-type MOFs decorated with single-atom Cu at different locations were synthesized according to the previous literatures with a slight modification. Fig. S1 schematically illustrated the synthesis procedure of single-atom Cu decorated UiO-66/UiO-67 and displayed their atomic structures of model units. Briefly, Cu/UiO-66 and UiO-67-Cu_N were fabricated through anchoring the Cu(II) ions to the defect sites of UiO-66 and the ligand of UiO-67-bpydc, respectively. Cu_{ex}-UiO-66, where the Cu atoms were anchored on the node of UiO-66, was achieved by using mixed metal precursors *via* a simple solvothermal method. The detailed synthetic procedures were illustrated in supporting information. Firstly, the morphology of the as-fabricated single-atom Cu decorated UiO-66/UiO-67 was characterized by transmission electron microscopy (TEM) and according to the TEM images as depicted in Fig. 1a-c&Fig. S2, the three MOFs showed nearly bipyramidal structures with a diameter of about 80–100 nm. Their corresponding energy-dispersive spectroscopy (EDS) mapping images indicated the uniform dispersion of Cu and Zr in all the as-fabricated MOFs (Fig. 1d-f).

To reveal the local coordination structures of the incorporated Cu atoms in these MOFs, X-ray absorption spectroscopy (XAS) measurement was further conducted. The Cu K-edge X-ray absorption near edge structure (XANES) spectra in Fig. S3a-c showed very close absorption edge to that of CuO and Cu_2O, demonstrating the Cu species is mixed valence state including both Cu^+ and Cu^{2+}. The corresponding fitting results of Fourier transformed extended X-ray absorption fine structure (EXAFS) spectra presented a dominated peak at 1.9 Å assigned to Cu-O/Cu-N scattering path and no peak related to Cu-Cu bond was observed, with the fitting results summarized in Fig. 1g-i and Table S1, proving the Cu species was single-atomically dispersed in UiO-type MOFs.

Moreover, combing with the nuclear magnetic resonance (NMR) spectroscopy, X-ray diffraction (XRD) pattern, and Fourier Transform Infrared (FTIR) spectroscopy, the precise structural information of the incorporated Cu atoms was acquired, achieving the identification of the location of Cu sites. In detail, the characteristic peak around 3000–3500 cm^{-1} in the FTIR spectrum (Fig. S4a), assigned to the terminal -OH/-OH_2 groups on the Zr_6-oxo, was apparently decreased after the incorporation of Cu atoms, revealing the interaction of Cu with −OH/−OH_2 groups terminating the defect sites. The EXAFS spectrum of

Cu/UiO-66 shown in Fig. 1g reflected a distance of the main backscattering shell of 1.96 ± 0.03 Å, assigned to a Cu-O shell with an average coordination number of 1.6 (Table S1). It is reasonable that the unsaturated coordinated Cu atom was bound to the missing-linker defect sites and various atomic structures are presented in Scheme 1 A(a). In addition, the XRD pattern of Cu/UiO-66 (Fig. S4b) mainly exhibited characteristic peaks of typical UiO-66, demonstrating the stable configuration. Therefore, the proposed Cu/UiO-66, where the Cu atom was attached on the missing-linker defect sites, has been successfully prepared. As for Cu_{ex}-UiO-66, the characteristic peaks of UiO-66 disappeared in the XRD pattern of Cu_{ex}-UiO-66 (Fig. S5a), demonstrated the different location of the incorporated Cu atoms from the defect sites. Moreover, the main backscattering of Cu-O was observed at 1.92 ± 0.03 Å and the average coordination number of Cu was estimated to be 2.8, implying the nearly saturated Cu atom. Theoretically, a 4-coordinated exchanged-in Cu^{II} ion cannot act as the originally present 8-coordinated Zr^{IV} ions and therefore, the incorporation of Cu^{II} might lead to a change in the configuration of MOF from octahedron to tetrahedron. [41–43] Meanwhile, the incorporation of low-coordinated Cu atoms could result in additional missing linkers in the Cu-exchanged version of the MOF. Accordingly, an increase of oxygen vacancy was found for Cu_{ex}-UiO-66 in compared to UiO-66 (Fig. S5b). Based on the above analysis, it is reasonable that the Cu atoms are mainly anchored on the nodes for Cu_{ex}-UiO-66. In case of UiO-67-Cu_N, a similar XRD pattern to the native UiO-67-bpydc was observed (Fig. S6a) and there appeared the characteristic peak of the typical stretching vibration of C-N bond around 2245 cm^{-1} in the FTIR spectrum (Fig. S6b), which was disturbed after the incorporation of Cu species. Moreover, the chemical shift and the intensity of the H in the benzene ring of the ligand in UiO-67-Cu_N were changed compared with that of UiO-67-bpydc (Fig. S6c&d), indicating that the Cu atom was anchored on the ligand of MOF. [44] The average coordination number of Cu was estimated to be 2.5 from the EXAFS analysis (Table S1), suggesting that Cu atom was coordinated by two N atoms in ligand and the local coordination model was shown in Scheme 1 A(c). Therefore, the three UiO-type MOFs decorated with single-atom Cu at different locations have been successfully prepared through identifying the location structure and coordination environment of Cu site.

Next, the valence states of Cu in the as-prepared MOFs were elucidated using X-ray photoelectron spectroscopy (XPS). The XPS spectra in Fig. 1j-l revealed the presence of Cu, Zr, and O in all the as-prepared MOFs, in agreement with the EDS mapping images (Fig. 1d-f). Then the high resolution XPS spectra displayed the Cu 2p peak in Fig. 1j-l (inset) can be divided into two main peaks at 932.2 eV and 934.8 eV, which can be well assigned to the Cu(I) and Cu(II) species. Besides, the Cu loading amounts in these MOFs were close according to inductively coupled plasma atomic emission (ICP-AES) analysis (Table S2). The successful construction of Cu/UiO-66, Cu_{ex}-UiO-66 and UiO-67-Cu_N with well-defined location of the incorporated catalytic sites provides an ideal platform to study the spatial-position effect of the catalytic sites on the catalytically hydrolytic performance of MOF-based nanozymes.

3.2. The catalytic hydrolysis of the phosphoester bond by UiO-type MOFs decorated with single-atom Cu at different spatial locations

After successful fabrication of a series of single-atom Cu decorated UiO-66/UiO-67, the hydrolysis of the phosphoester bond by the as-prepared MOFs was quantitatively evaluated using dimethyl-4-nitrophenyl phosphate (DMNP) as a model hydrolysis substrate (Fig. 2a). The catalytically hydrolytic reaction yields a yellow-colored product (*p*-nitrophenol with $\lambda_{max} = 407$ nm), which can be conveniently monitored and quantified by a UV–vis spectrophotometer. For comparison, the steady-state kinetic analysis was carried out at various concentrations of DMNP. By plotting the initial reaction velocities against DMNP concentration, typical Michaelis-Menten-type saturation kinetic curves were observed (Fig. 2b), indicating that the introduction
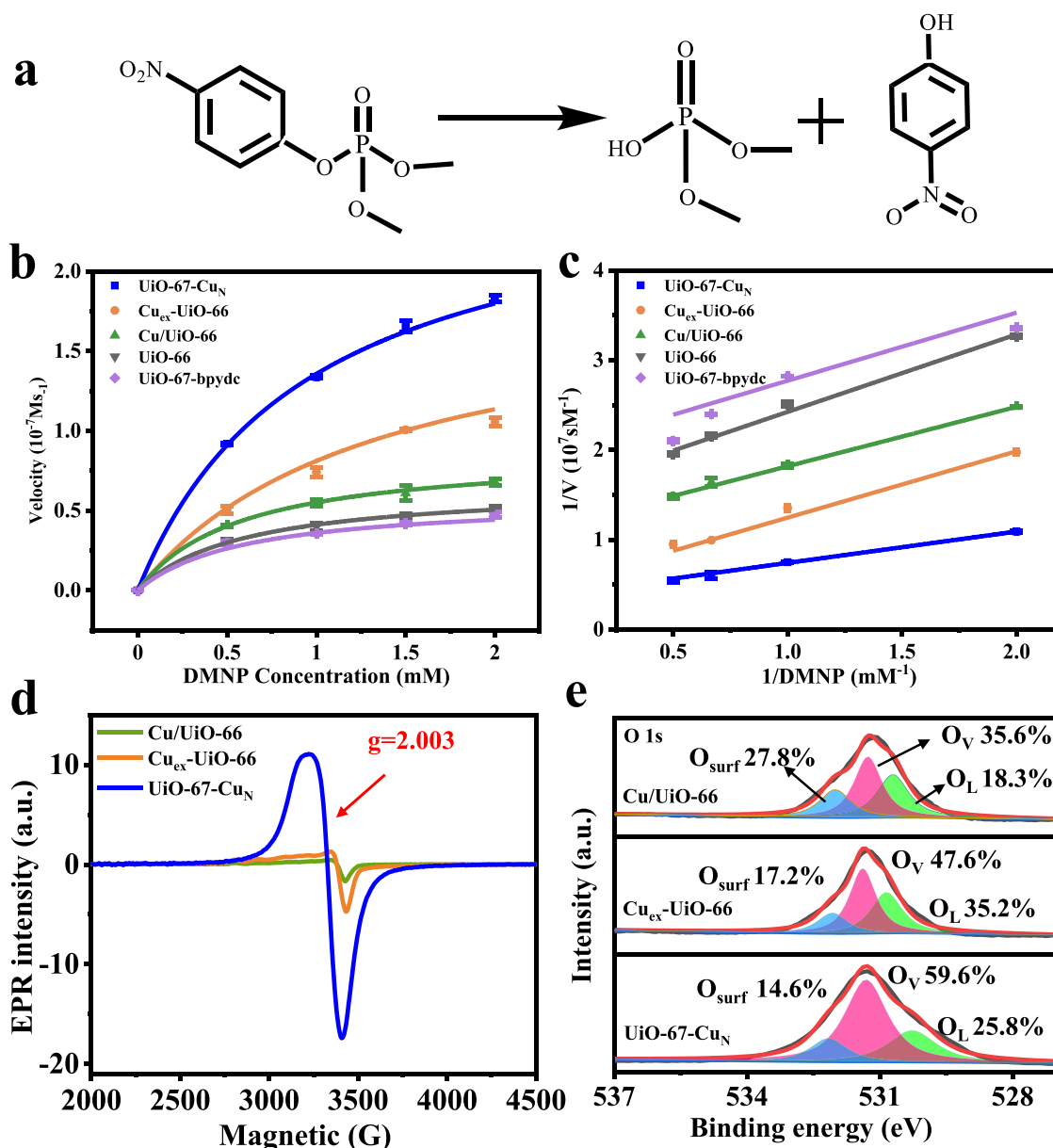
Fig. 2. The hydrolysis activity of the phosphoester bond by a series of single-atom Cu decorated UiO-type MOFs. (a) A scheme of the hydrolysis reaction of DMNP. (b) Steady-state kinetic assay of the three MOFs by varying the concentrations of DMNP. (c) The corresponding double reciprocal curves for determining kinetic constants of the three MOFs for DMNP substrate. (d) EPR spectra of the three MOFs. (e) The O 1 s XPS spectra of the three MOFs. O_L, O_v, and O_{surf} are corresponding to lattice oxygen, oxygen vacancy, and surface-absorbed water/hydroxyl groups, respectively.

of Cu promoted the hydrolysis activity of UiO-type MOFs. Besides, it was notable that the as-prepared MOFs exhibited higher hydrolysis activity toward phosphoester bonds than that of most reported MOFs (Fig. S7) and CeO$_2$ nanoparticles (Fig. S8&Tabel S3). Moreover, the product inhibition effect disappeared, which was generally observed for CeO$_2$ and metal complex-based phosphatase mimetics. [18,19] It is suggested that UiO-type MOFs excellent alternatives to natural phosphatase.

Furthermore, the Michaelis-Menten-type curves were then converted to the double-reciprocal plots (Fig. 2c), from which the K_{cat} values along with other kinetic parameters were summarized (Table 1). Strikingly, the three kinds of single-atom Cu decorated UiO-type MOFs showed distinctly different catalytic activity. Specifically, the maximum initial velocity (V_{max}) value toward the hydrolysis of DMNP catalyzed by Cu/UiO-66 was approximately 1.32 times higher than that catalyzed by UiO-66, whereas UiO-67-Cu$_N$ increase the V_{max} up to 4.03-fold. Overall, the UiO-67-Cu$_N$ displayed the most superior hydrolysis activity among

Table 1
Comparison of the kinetic parameters of a series of MOFs toward the hydrolysis of DMNP.

Sample	[S] (mM)	K_m (mM)	V_{max} (10^{-7} M·s^{-1})	K_{cat} (10^{-4} s^{-1})	K_{cat}/K_m (10^{-4} m·M^{-1}·s^{-1})	$t_{1/2}$ (h)
UiO-66	0.5	1.19	0.66	1.32	1.11	1.46
Cu/UiO-66	0.5	1.16	0.87	1.74	1.5	1.1
Cu$_{ex}$-UiO-66	0.5	2.66	1. 89	3.78	1.42	0.51
UiO-67-Cu$_N$	0.5	1.93	2.66	5.32	2.76	0.36

the three MOFs. In addition, the effects of pH and temperature on the enzymatic hydrolysis activity of the prepared MOFs were studied through subjecting the catalyst to different pH values and temperatures. The as-prepared MOFs can exhibit excellent catalytic activity over a broad pH and temperature range (Fig. S9). Especially, the as-prepared MOFs still displayed high catalytic efficiencies under weak acidic conditions, which greatly enhanced their environmental adaptability and will be more beneficial for practical applications. Besides, the stability of the as-prepared MOFs and natural alkaline phosphatase (ALP) was compared. As shown in Fig. S10, the natural ALP sharply lost its activity and dropped to only 60% left on the 2nd day, while the as-prepared MOFs maintained nearly 80% even full activity at the 4th day.

3.3. Regulation mechanism for the Cu location-dependent hydrolysis activity of UiO-type MOFs

To reveal the origin of the outstanding catalytic activity of UiO-67-Cu_N, electron paramagnetic resonance (EPR) was used to investigate the coordinatively unsaturated defects within the prepared MOFs. As shown in Fig. 2d, a symmetrical signal was observed at g= 2.003 in the ESR spectra of the as-prepared MOFs, which can be assigned to the typical signal of oxygen vacancies. Meanwhile, the intensity of the signal showed a similar trend with that of the hydrolysis activity. In compared to a weak signal of Cu/UiO-66, an increase of signal intensity was found for Cu_{ex}-UiO-66. Notably, UiO-67-Cu_N displayed remarkably enhanced signal. It is indicated that the differential hydrolysis activity of the three kinds of UiO-type MOFs might be attributed to the difference in the level of oxygen vacancies originated from the incorporation of Cu atoms on different locations.

The oxygen vacancies in UiO-type MOFs are generally formed by losing lattice oxygen atoms. [45,46] Therefore, a detailed study on the O 1 s XPS spectra of the prepared MOFs was further performed. The O1s peak in Fig. 2e can be divided into three peaks at 530.2, 531.3, 532.1 eV, which are assigned to three oxygen forms: lattice oxygen (O_L), oxygen vacancies located near oxygen lattice sites (O_V), surface oxygen species (O_{surf}), respectively. The ratio of O_V/O_{Total} followed the order of Cu/UiO-66 <Cu_{ex}-UiO-66 <UiO-67-Cu_N, in accordance with the trend of the ESR results and UiO-67-Cu_N with the strongest hydrolysis activity had the highest concentration of O_V among the three as-prepared MOFs. It is concluded that the oxygen vacancy, especially, the percentage of O_V accounting for O_{Total} is an important parameter that influences the hydrolysis activity of UiO-type MOFs.

Apart from oxygen vacancies in the MOFs, the activity of Zr^{IV} ions in the MOFs regulated by the location of the incorporated Cu atoms also has great effects on their hydrolysis activity. For example, the Cu_{ex}-UiO-66 exhibited high catalytic activity than Cu/UiO-66, which was consistent with our original hypothesis that tetrahedral Zr^{IV} ions in the Cu_{ex}-UiO-66 should be more active than the more saturated octahedral Zr^{IV} ions in the Cu/UiO-66. This is because more "missing linkers" defects, even maybe "missing cluster" defects would be generated in the Cu_{ex}-UiO-66, further enlarging the surface area of MOFs and improving the catalytic performance. Similarly, owing to the highest concentration of oxygen defects, it would be more beneficial to promote the hydrolytic activity of Zr^{IV} ions in the UiO-67-Cu_N, further enhancing the hydrolytic activity.

Taking advantages of the high accessibility to substrate molecules through incorporating catalytic sites into organic linkers, the activity of Cu catalytic sites in UiO-67-Cu_N also played an important role on their hydrolysis activity. The XPS analysis also demonstrated that the three MOFs exhibited different Cu^{2+}/Cu^+ ratios and UiO-67-Cu_N held the most $Cu^{(II)}$ species, confirming the most Lewis acid sites. [47,48] Thus, the elevated Lewis acidity caused by high oxidation state contributes to nucleophilic attack and activating the phosphoester bond. A plausible mechanism of the superior activity of UiO-67-Cu_N may include more effective metal-hydroxide attack to the phosphoester bond combined with high accessibility of the substrate and the synergistic effect

between dual catalytic sites, together promoting the hydrolytic performance.

All the results suggested that the hydrolysis activity of the as-prepared MOFs could be enhanced through incorporation of single-atom Cu and tuning their locations. When Cu atom was anchored on the ligand, the fabricated UiO-67-Cu_N exhibited the highest hydrolysis activity toward the phosphoester bond. Moreover, the main regulation mechanism can be proposed, that is the high concentration of oxygen vacancy and elevated Lewis acidity contribute to the hydrolysis activity of the as-prepared MOFs.

3.4. DNA cleavage activity of UiO-67-Cu_N

To evaluate the cleavage performance of DNA by the as-fabricated MOFs, the UiO-67-Cu_N with the most superior hydrolytic activity was selected as model subjects and firstly investigated their catalytically hydrolytic activity on the model substrates of phosphodiester bond (bis (4-nitrophenl) phosphate, BNPP). [49,50] Similarly, the catalytic activity of UiO-67-Cu_N on the BNPP hydrolysis was evaluated by determining the absorption of the products (*p*-nitrophenol, *p*-NP) at 407 nm. As shown in Fig. S11, the absorption of *p*-NP increased gradually along with the increase of reaction time.

Afterwards, the practicality of UiO-67-Cu_N in hydrolysis of small single-strand DNA was investigated by polyacrylamide gel electrophoresis. The single-strand DNA bands disappeared after treatment with UiO-67-Cu_N, while the UiO-66 and UiO-67-bpydc showed negligible hydrolytic effect on the single-strand DNA (Fig. S12), demonstrating the excellent DNA hydrolytic activity of UiO-67-Cu_N. Next, we examined the hydrolytic activity of UiO-67-Cu_N on plasmid DNA. Consistently, Fig. 3a showed that the bands of plasmid DNA gradually became weaker until disappeared as the exposure concentration of UiO-67-Cu_N increased, which indicated that the plasmid DNA was also effectively degraded by UiO-67-Cu_N. The quantitative analysis showed that UiO-67-Cu_N exhibited a concentration-dependent DNA hydrolytic activity and the plasmid DNA could be completely degraded when the concentration of UiO-67-Cu_N was increased up to 0.5 mg·mL^{-1} (Fig. 3b). We next examined the surface topography of the plasmids using the atomic force microscope (AFM). As shown in Fig. 3c, plasmid DNA was closed circular in the untreated control, however, upon exposure to UiO-67-Cu_N, the plasmids were damaged and only short fragments of DNA were observed upon exposure to 0.5 mg·mL^{-1} UiO-67-Cu_N. In compared to the height of untreated plasmid DNA, the measured height of DNA after treatment with UiO-67-Cu_N was significantly lower than 0.5 nm, indicating that the typical superhelix morphology completely disappeared and the plasmid DNA was broken into small fragments. Both the gel electrophoresis and AFM results fully confirmed that the plasmid DNA was efficiently cleaved by UiO-67-Cu_N, which is a promising DNA hydrolase candidate.

3.5. Environmental adaptability of UiO-67-Cu_N

From the perspective of practical application, the excellent adaptation of nanomaterials to a wide range of environmental conditions is greatly essential. Therefore, the environmental adaptability of UiO-67-Cu_N was measured through subjecting the MOFs to different pH, a range of metal and salt ions and environmental water. The agarose gel electrophoresis in Fig. S13 showed that the UiO-67-Cu_N exhibited high DNA cleavage performance over a broad range of pH. Besides, ion is one of most common environmental stress factors and the MOFs would inevitably encounter various ions once exposed to the natural environment. Then, in the presence of metal ions (Na^+, K^+, Mg^{2+}, Ca^{2+}) and salt ions (Cl^-, CO_3^{2-}, NO_3^-), the DNA cleavage activity of MOFs was evaluated and as shown in Fig. 3e& S14, no significant changes of the hydrolysis activity of UiO-67-Cu_N towards DNA were observed under a range of ions. Similarly, the UiO-67-Cu_N maintained high activity without significant loss of activity in real water samples (Fig. S15). Moreover, the
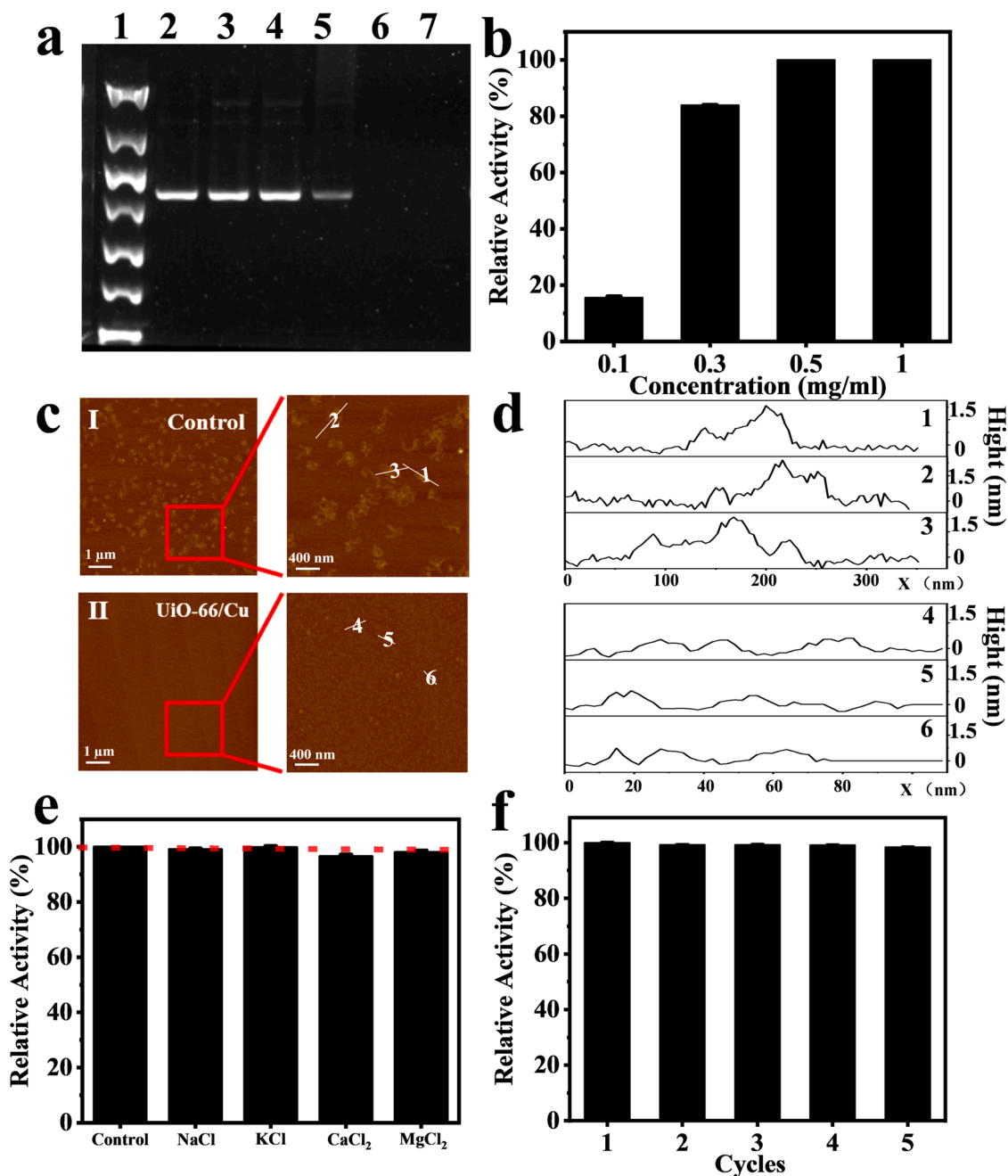
Fig. 3. DNA cleavage activity of UiO-67-Cu$_N$. (a) The gel electrophoresis analysis of plasmid DNA after treatment of different concentration of UiO-67-Cu$_N$. Lane 1 represents marker. Lanes 2 and 3 represent the control group, Lanes 4–7 represent the plasmid DNA after exposure to UiO-67-Cu$_N$ at the concentrations of 0.1, 0.3, 0.5 and 1 mg·mL^{-1}, respectively. (b) Effect of the UiO-67-Cu$_N$ concentration on the cleavage of plasmid DNA. The cleavage yields were achieved by the ratio between the product band and the total band intensity. (c) AFM images showing the cleavage of plasmid DNA by UiO-67-Cu$_N$. (d) Height analysis of plasmid DNA through AFM. (e) The DNA cleavage activity of UiO-67-Cu$_N$ in different ions. (f) The reusability of UiO-67-Cu$_N$.

reusability of an enzyme mimic is also critical for its potential application in practical application. As presented in Fig. 3f, the residual activity of UiO-67-Cu$_N$ still retained above 95% after reusing it five times. The high environmental stability, adaptability and reusability of UiO-67-Cu$_N$ offer an excellent opportunity for their practical environmental applications.

3.6. The extraction and cleavage of ARGs-carrying plasmids

The induced Penicillin-resistant *E. coli* cells were acquired through a long-term exposure to gradually increased concentrations of Penicillin sodium. The ARGs-carrying plasmid DNA was isolated and purified from the antibiotic-resistant *E. coli* according to manufacturers' protocols. The ARGs-carrying plasmid DNA was further identified through the ARGs transformation experiment as presented in Fig. 4a. There observed numerous transformants cultured on the Penicillin G-containing plates, indicating that the purified plasmid DNA containing antibiotic-resistance gene was successfully extracted (Fig. S16). Next, the ARGs-carrying plasmid DNA was respectively characterized by AFM and agarose gel electrophoresis (Fig. S17). Similarly, the band of ARGs-carrying plasmid DNA became weaker and finally disappeared after the treatment of UiO-67-Cu$_N$ (Fig. S18a), with a cleavage efficiency of 90% upon exposure to 0.3 mg·mL^{-1} UiO-67-Cu$_N$ (Fig. S18b).
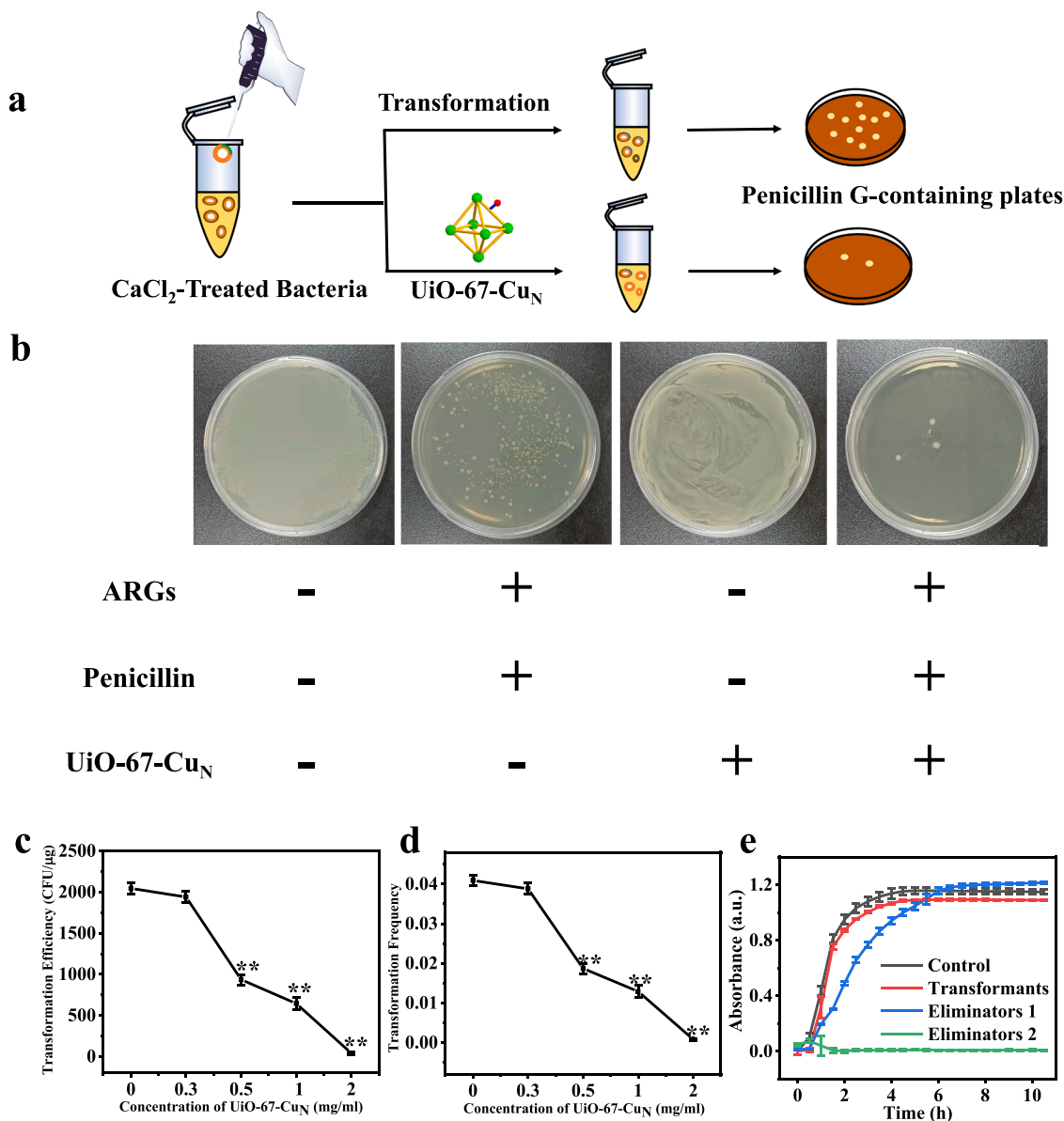
Fig. 4. The inhibitory effect of UiO-67-Cu$_N$ on the transformation of ARGs. (a) A schematic diagram of the transformation experiment of ARGs. (b) Representative photos of bacterial colonies in different incubation systems. (c) Effects of UiO-67-Cu$_N$ on the transformation efficiency of ARGs in plasmids. (d) Effects of UiO-67-Cu$_N$ on the transformation frequency of ARGs in plasmids. (e) The grow curve of the cells after different treatments. The control group and the Eliminators 1 group: the bacteria were cultured in the antibiotic-free LB medium, the Transformants group and the Eliminators 2 group: the bacteria were cultured in the LB medium containing Penicillin G.

3.7. The inhibitory effect of UiO-67-Cu$_N$ on the transformation of ARGs

The transformation achieved by direct uptake of eARGs (extracellular antibiotic-resistant genes) to competent bacteria is one of the important pathways of disseminating ARGs in the natural environment. Therefore, it is particularly important to systematically investigate the effect of UiO-67-Cu$_N$ on the transformation of eARGs and ARG-carrying plasmid DNA was chosen as the simulated eARGs in the environment. In order to exclude the inference of the possible inhibition effect of UiO-67-Cu$_N$ on bacterial growth, the antibacterial activity of UiO-67-Cu$_N$ was investigated. As shown in Fig. S19, no obvious inhibition of *E. coli* survival was observed at the UiO-67-Cu$_N$ concentrations up to 2 mg·mL^{-1}. Then we evaluated the influence of UiO-67-Cu$_N$ at 0–2 mg·mL^{-1} on the horizontal gene transfer of ARGs *via* transformation in *E. coli* cells. As a result, there were almost no transformants cultured on the Penicillin G-containing plates after the incubation both with UiO-67-Cu$_N$ and the

ARG-carrying plasmid DNA, indicating UiO-67-Cu$_N$ significantly inhibited the transformation of ARGs carried in the plasmid DNA (Fig. 4b). The transformation efficiency decreased gradually with the increase of the concentration of UiO-67-Cu$_N$ from 0.3 to 2 mg·mL^{-1} and the transformation of ARGs-carrying plasmid DNA could be completely inhibited at 2 mg·mL^{-1} UiO-67-Cu$_N$. As presented in Fig. 4d, with the concentration of UiO-67-Cu$_N$ increased, the transformation frequency decreased from 0.04 to 0.0008, further confirming that the HGT of ARG-carrying plasmid DNA into the *E. coli* cells was effectively limited by UiO-67-Cu$_N$. Next, the effect of UiO-67-Cu$_N$ on the elimination of antibiotic resistance was evaluated through the determination of the grow curve of the cells (transformants and eliminators) after the ARGs transformation experiments. As shown in Fig. 4e, bacteria without treatment with UiO-67-Cu$_N$ normally grew in the antibiotic-resistant LB medium with or without Penicillin G. Instead, no substantial growth of the eliminator was observed in the Penicillin G-containing LB medium,

while the growth curve of the eliminator in the normal LB medium was similar to that of transformants, demonstrating the elimination of bacterial resistance to antibiotic. All the above results indicated that UiO-67-Cu$_N$ with superior DNA-hydrolytic activity could efficiently inhibit the horizontal gene transfer of ARGs and eliminate bacterial resistance to antibiotic.

4. Conclusions

In summary, we have successfully synthesized three kinds of UiO-type MOFs decorated with single-atom Cu at the different locations and investigated the spatial position effects of the incorporated Cu atom on the hydrolysis activity of phosphoester bonds by UiO-type MOFs. A comprehensive analysis of the local structure of the single-atom Cu sites in MOFs was performed by applying XAS and NMR methods, different locations of Cu atoms were respectively identified including occupying the defect sites, as part of the node and attachment to the ligand. Next, the hydrolysis activity toward the phosphoester bond by MOFs was evaluated using model reaction and interestingly, the three kinds of UiO-type MOFs displayed distinctly hydrolytic activity. Remarkably, through anchoring the Cu atoms on the ligand of MOF, UiO-67-Cu$_N$ exhibited the highest activity among the three MOFs. In order to explore the potential modulation mechanism, the chemical state of Cu atom and the surface defect of UiO-type MOFs were respectively characterized using EPR and XPS. As a result, UiO-67-Cu$_N$ has the highest density of oxygen vacancy and the strongest Lewis acidity. Therefore, tuning the location of the incorporated metal atoms in MOFs results in the change of oxygen vacancies and Lewis acidity of MOFs, which might be a promising modulation strategy for enhancing the activity of MOF-based nanozymes. To our knowledge, this is the first systematic study on the spatial position effect of the incorporated catalytic sites on the catalytic hydrolysis activity of MOFs. Moreover, the optimized UiO-67-Cu$_N$ displayed excellent DNA cleavage performance under various environmental conditions, demonstrating excellent environment adaptability. As expected, the transformation of ARGs to sensitive bacteria was effectively inhibited after treatment with UiO-67-Cu$_N$ and bacteria resistance to antibiotic was simultaneously eliminated. This study not only provides new strategy for optimization of the hydrolytic activity of MOF-based nanozymes, but also advances the explorations on new approaches for the removal of ARGs with high efficiency and low pollution.

Supporting information

Materials, synthesis of UiO-66, UiO-67 and detailed sample preparation for materials characterization are described in the Supplemental Information. General procedure for evaluating the environmental adaptability and DNA cleavage activity of the MOF-based nanozymes can also be found in the Supplemental Information.

CRediT authorship contribution statement

Ge Fang: Conceptualization, Methodology, Investigation, Formal analysis, Writing – original draft, Funding acquisition. **Ruonan Kang:** Investigation, Resources, Data curation, Visualization. **Yu Chong:** Investigation. **Liming Wang:** Investigation. **Chuanqiang Wu:** Investigation. **Cuicui Ge:** Conceptualization, Writing – review & editing, Supervision, Project administration, Funding acquisition.

Declaration of Competing Interest

The authors declare that they have no known competing financial interests or personal relationships that could have appeared to influence the work reported in this paper.

Data Availability

Data will be made available on request.

Appendix A. Supporting information

Supplementary data associated with this article can be found in the online version at doi:10.1016/j.apcatb.2022.121931.

References

[1] Y.G. Zhu, Y. Zhao, B. Li, C.L. Huang, S.Y. Zhang, S. Yu, Y.S. Chen, T. Zhang, M. R. Gillings, J.Q. Su, Continental-scale pollution of estuaries with antibiotic resistance genes, Nat. Microbiol. 2 (4) (2017) 16270.

[2] T.U. Berendonk, C.M. Manaia, C. Merlin, D. Fatta- Kassinos, E. Cytryn, F. Walsh, H. Bürgmann, H. Sørum, M. Norström, M.-N. Pons, N. Kreuzinger, P. Huovinen, S. Stefani, T. Schwartz, V. Kisand, F. Baquero, J.L. Martinez, Tackling antibiotic resistance: the environmental framework, Nat. Rev. Microbiol. 13 (5) (2015) 310–317.

[3] Z. Zhang, Q. Zhang, T. Wang, N. Xu, T. Lu, W. Hong, J. Penuelas, M. Gillings, M. Wang, W. Gao, H. Qian, Assessment of global health risk of antibiotic resistance genes, Nat. Commun. 13 (1) (2022), 1553-1553.

[4] S. Shao, Y. Hu, J. Cheng, Y. Chen, Research progress on distribution, migration, transformation of antibiotics and antibiotic resistance genes (ARGs) in aquatic environment, Crit. Rev. Biotechnol. 38 (8) (2018) 1195–1208.

[5] H. Gao, L. Zhang, Z. Lu, C. He, Q. Li, G. Na, Complex migration of antibiotic resistance in natural aquatic environments, Environ. Pollut. 232 (2018) 1–9.

[6] D. Sun, K. Jeannot, Y. Xiao, C.W. Knapp, Editorial: Horizontal gene transfer mediated bacterial antibiotic resistance, Front. Microbiol. 10 (2019), 1933-1933.

[7] S. Li, C. Zhang, F. Li, T. Hua, Q. Zhou, S.H. Ho, Technologies towards antibiotic resistance genes (ARGs) removal from aquatic environment: a critical review, J. Hazard. Mater. 411 (2021) 125148.

[8] L. Ma, H. Yang, L. Guan, X. Liu, T. Zhang, Risks of antibiotic resistance genes and antimicrobial resistance under chlorination disinfection with public health concerns, Environ. Int. 158 (2022), 106978.

[9] C.S. Zhou, J.W. Wu, L.L. Dong, B.F. Liu, D.F. Xing, S.S. Yang, X.K. Wu, Q. Wang, J. N. Fan, L.P. Feng, G.L. Cao, Removal of antibiotic resistant bacteria and antibiotic resistance genes in wastewater effluent by UV-activated persulfate, J. Hazard. Mater. 388 (2022) 122070.

[10] Q. Qiu, G. Li, Y. Dai, Y. Xu, P. Bao, Removal of antibiotic resistant microbes by Fe (II)-activated persulfate oxidation, J. Hazard. Mater. 396 (2022) 122733.

[11] H. Yin, X. Chen, W. Wang, P.K. Wong, H. Zhao, T. An, Accelerated evolution of bacterial antibiotic resistance through early emerged stress responses driven by photocatalytic oxidation, Appl. Catal. B: Environ. 269 (2022), 118829.

[12] Z. Zhou, Z. Shen, Z. Cheng, G. Zhang, M. Li, Y. Li, S. Zhan, J.C. Crittenden, Mechanistic insights for efficient inactivation of antibiotic resistance genes: a synergistic interfacial adsorption and photocatalytic-oxidation process, Sci. Bull. 65 (24) (2020) 2107–2119.

[13] J. Fang, L. Jin, Q. Meng, S. Shan, D. Wang, D. Lin, Biochar effectively inhibits the horizontal transfer of antibiotic resistance genes *via* transformation, J. Hazard. Mater. 423 (2022), 127150.

[14] T. Zhang, Y. Hu, L. Jiang, S. Yao, K. Lin, Y. Zhou, C. Cui, Removal of antibiotic resistance genes and control of horizontal transfer risk by UV, chlorination and UV/chlorination treatments of drinking water, Chem. Eng. J. 358 (2019) 589–597.

[15] R. Fang, J. Liu, Cleaving DNA by nanozymes, J. Mater. Chem. B 8 (32) (2020) 7135–7142.

[16] F. Li, S. Li, X. Guo, Y. Dong, C. Yao, Y. Liu, Y. Song, X. Tan, L. Gao, D. Yang, Chiral carbon dots mimicking topoisomeraseI to mediate the topological rearrangement of supercoiled DNA enantioselectivity, Angew. Chem. Int. Ed. 59 (27) (2020) 11087–11092.

[17] J. Zhang, S. Wu, L. Ma, P. Wu, J. Liu, Graphene oxide as a photocatalytic nuclease mimicking nanozyme for DNA cleavage, Nano Res. 13 (2) (2020) 455–460.

[18] H. Liu, J. Liu, Self-limited phosphatase-mimicking CeO$_2$ nanozymes, ChemNanoMat 6 (6) (2020) 947–952.

[19] M. Zandieh, J. Liu, Nanozyme catalytic turnover and self-limited reactions, ACS Nano 15 (10) (2021) 15645–15655.

[20] L. Jiang, Y. Sun, Y. Chen, P. Nan, From DNA to nerve agents – the biomimetic catalysts for the hydrolysis of phosphate esters, ChemistrySelect 5 (30) (2020) 9492–9516.

[21] Y.H. Cheung, K. Ma, M.C. Wasson, X. Wang, K.B. Idrees, T. Islamoglu, J. Mahle, G. W. Peterson, J.H. Xin, O.K. Farha, Environmentally benign biosynthesis of hierarchical MOF/bacterial cellulose composite sponge for nerve agent protection, Angew. Chem. Int. Ed. (2022), e202202207.

[22] S.S. Sandhu, Y.G. Kotagiri, P.U.A.I. Fernando I, M. Kalaj, N. Tostado, H. Teymourian, E.M. Alberts, T.L. Thornell, G.R. Jenness, S.P. Harvey, S.M. Cohen, L.C. Moores, J. Wang, Green MIP-202(Zr) catalyst: degradation and thermally robust biomimetic sensing of nerve agents, J. Am. Chem. Soc. 143 (43) (2021) 18261–18271.

[23] Y. Liu, A.J. Howarth, N.A. Vermeulen, S.Y. Moon, J.T. Hupp, O.K. Farha, Catalytic degradation of chemical warfare agents and their simulants by metal-organic frameworks, Coord. Chem. Rev. 346 (2017) 101–111.

[24] K. Vellingiri, L. Philip, K.H. Kim, Metal-organic frameworks as media for the catalytic degradation of chemical warfare agents, Coord. Chem. Rev. 353 (2017) 159–179.

[25] Y. Bai, Y. Dou, L.H. Xie, W. Rutledge, J.R. Li, H.C. Zhou, Zr-based metal-organic frameworks: design, synthesis, structure, and applications, Chem. Soc. Rev. 45 (8) (2016) 2327–2367.

[26] M.J. Katz, J.E. Mondloch, R.K. Totten, J.K. Park, S.T. Nguyen, O.K. Farha, J. T. Hupp, Simple and Compelling Biomimetic Metal-organic framework catalyst for the degradation of nerve agent simulants, Angew. Chem. Int. Ed. 53 (2) (2014) 497–501.

[27] E. López-Maya, C. Montoro, L.M. Rodríguez-Albelo, S.D. Aznar Cervantes, A. A. Lozano-Pérez, J.L. Cenís, E. Barea, J.A.R. Navarro, Textile/metal-organic-framework composites as self-detoxifying filters for chemical-warfare agents, Angew. Chem. Int. Ed. 54 (23) (2015) 6790–6794.

[28] S.Y. Moon, Y. Liu, J.T. Hupp, O.K. Farha, Instantaneous hydrolysis of nerve-agent simulants with a six-connected zirconium-based metal-organic framework, Angew. Chem. Int. Ed. 54 (23) (2015) 6795–6799.

[29] I. Nath, J. Chakraborty, F. Verpoort, Metal organic frameworks mimicking natural enzymes: a structural and functional analogy, Chem. Soc. Rev. 45 (15) (2016) 4127–4170.

[30] Y. Wang, Z. Liu, H. Zhang, J. Liu, H. Dai, T. Ji, F. Liu, P. Cao, J. Zou, S. Wang, L. Wang, Z. Wang, MOF effectively deliver CRISPR and enhance gene-editing efficiency via MOF's hydrolytic activity of phosphate ester bonds, Chem. Eng. J. 439 (2022), 134992.

[31] A. Loosen, F. de Azambuja, S. Smolders, J. Moons, C. Simms, D. De Vos, T.N. Parac-Vogt, Interplay between structural parameters and reactivity of Zr_6-based MOFs as artificial proteases, Chem. Sci. 11 (26) (2020) 6662–6669.

[32] H.G.T. Ly, G. Fu, F. de Azambuja, D. De Vos, T.N. Parac-Vogt, Nanozymatic activity of UiO-66 metal-organic frameworks: tuning the nanopore environment enhances hydrolytic activity toward peptide bonds, ACS Appl. Nano Mater. 3 (9) (2020) 8931–8938.

[33] R.J. Young, M.T. Huxley, E. Pardo, N.R. Champness, C.J. Sumby, C.J. Doonan, Isolating reactive metal-based species in Metal–Organic Frameworks -viable strategies and opportunities, Chem. Sci. 11 (16) (2020) 4031–4050.

[34] M.R. Mian, H. Chen, R. Cao, K.O. Kirlikovali, R.Q. Snurr, T. Islamoglu, O.K. Farha, Insights into catalytic hydrolysis of organophosphonates at M-OH sites of azolate-based metal organic frameworks, J. Am. Chem. Soc. 143 (26) (2021) 9893–9900.

[35] T. Islamoglu, A. Atilgan, S.-Y. Moon, G.W. Peterson, J.B. DeCoste, M. Hall, J. T. Hupp, O.K. Farha, Cerium(IV) *vs* zirconium(IV) based metal-organic frameworks for detoxification of a nerve agent, Chem. Mater. 29 (7) (2017) 2672–2675.

[36] M. Zhang, J. Lou, R. Xu, P. Li, Y. Sha, H. Zhang, Y. Jia, Z. Chen, D. Wu, Y. Ling, Y. Zhou, Post-synthetic anchoring of Fe(III) into a fcu-type Zr-MOF for the catalyzed hydrolysis of 5-hydroxylmethoxyfurfural, Microporous Mesoporous Mater. 328 (2021), 111449.

[37] J. Castells-Gil, M. Padial, N. Almora-Barrios, N. Gil-San-Millán, R. Romero-Ángel, M. Torres, V. da Silva, I. Vieira, B.C.J. Waerenborgh, J.C. Jagiello, J. Navarro, J.A. R. Tatay, S. Martí-Gastaldo, C, Heterometallic titanium-organic frameworks as dual-metal catalysts for synergistic non-buffered hydrolysis of nerve agent simulants, Chem 6 (11) (2020) 3118–3131.

[38] E. López-Maya, N.M. Padial, J. Castells-Gil, C.R. Ganivet, A. Rubio-Gaspar, F. G. Cirujano, N. Almora-Barrios, S. Tatay, S. Navalón, C. Martí-Gastaldo, Selective implantation of diamines for cooperative catalysis in isoreticular heterometallic titanium–organic frameworks, Angew. Chem. Int. Ed. 60 (21) (2021) 11868–11873.

[39] A.M. Mageed, B. Rungtaweevoranit, M. Parlinska-Wojtan, X. Pei, O.M. Yaghi, R. J. Behm, Highly active and stable single-atom Cu catalysts supported by a metal–organic framework, J. Am. Chem. Soc. 141 (13) (2019) 5201–5210.

[40] H. Zheng, Z. Ji, K.R. Roy, M. Gao, Y. Pan, X. Cai, L. Wang, W. Li, C.H. Chang, C. Kaweeteerawat, C. Chen, T. Xia, Y. Zhao, R. Li, Engineered graphene oxide nanocomposite capable of preventing the evolution of antimicrobial resistance, ACS Nano 13 (10) (2019) 11488–11499.

[41] Y. Zhu, J. Zheng, J. Ye, Y. Cui, K. Koh, L. Kovarik, D.M. Camaioni, J.L. Fulton, D. G. Truhlar, M. Neurock, C.J. Cramer, O.Y. Gutiérrez, J.A. Lercher, Copper-zirconia interfaces in UiO-66 enable selective catalytic hydrogenation of CO_2 to methanol, Nat. Commun. 11 (1) (2020) 5849.

[42] H.G.T. Nguyen, L. Mao, A.W. Peters, C.O. Audu, Z.J. Brown, O.K. Farha, J.T. Hupp, S.T. Nguyen, Comparative study of titanium-functionalized UiO-66: support effect on the oxidation of cyclohexene using hydrogen peroxide, Catal. Sci. Technol. 5 (9) (2015) 4444–4451.

[43] A. Gómez-Avilés, M. Peñas-Garzón, J. Bedia, D.D. Dionysiou, J.J. Rodríguez, C. Belver, Mixed Ti-Zr metal-organic-frameworks for the photodegradation of acetaminophen under solar irradiation, Appl. Catal. B Environ. 253 (2019) 253–262.

[44] W.H. Chen, M. Vázquez-González, A. Kozell, A. Cecconello, I. Willner, Cu^{2+}-modified metal–organic framework nanoparticles: a peroxidase-mimicking nanoenzyme, Small 14 (5) (2018), 1703149.

[45] R. Xu, Q. Ji, P. Zhao, M. Jian, C. Xiang, C. Hu, G. Zhang, C. Tang, R. Liu, X. Zhang, J. Qu, Hierarchically porous UiO-66 with tunable mesopores and oxygen vacancies for enhanced arsenic removal, J. Mater. Chem. A 8 (16) (2020) 7870–7879.

[46] G. Ye, H. Wang, X. Zeng, L. Wang, J. Wang, Defect-rich bimetallic UiO-66(Hf-Zr): solvent-free rapid synthesis and robust ambient-temperature oxidative desulfurization performance, Appl. Catal. B Environ. 299 (2021), 120659.

[47] S. Li, Z. Zhou, Z. Tie, B. Wang, M. Ye, L. Du, R. Cui, W. Liu, C. Wan, Q. Liu, S. Zhao, Q. Wang, Y. Zhang, S. Zhang, H. Zhang, Y. Du, H. Wei, Data-informed discovery of hydrolytic nanozymes, Nat. Commun. 13 (1) (2022) 827.

[48] J. Yang, S. Hu, L. Shi, S. Hoang, W. Yang, Y. Fang, Z. Liang, C. Pan, Y. Zhu, L. Li, J. Wu, J. Hu, Y. Guo, Oxygen vacancies and lewis acid sites synergistically promoted catalytic methane combustion over perovskite oxides, Environ. Sci. Technol. 55 (13) (2021) 9243–9254.

[49] Y.H. Zhou, Z. Zhang, M. Patrick, F. Yang, R. Wei, Y. Cheng, J. Gu, Cleaving DNA-model phosphodiester with Lewis acid–base catalytic sites in bifunctional Zr–MOFs, Dalton Trans. 48 (23) (2019) 8044–8048.

[50] H. Hu, X. Kang, Z. Shan, X. Yang, W. Bing, L. Wu, H. Ge, H. Ji, A DNase-mimetic artificial enzyme for the eradication of drug-resistant bacterial biofilm infections, Nanoscale 14 (7) (2022) 2676–2685.